Orientation Mediated Enhancement on Magnetic Hyperthermia of Fe_3O_4 Nanodisc

*Yong Yang, Xiaoli Liu, Yunbo Lv, Tun Seng Herng, Xianhui Xu, Weixing Xia, Taishi Zhang, Jie Fang, Wen Xiao, and Jun Ding**

A two-step chemical approach to synthesize high quality Fe_3O_4 nanodisc is reported. The magnetic hyperthermia properties of the nanodisc and isotropic nanoparticles are investigated systematically. The results suggest that the nanodisc shows much higher specific absorption rate (SAR) than isotropic nanoparticles. This is attributed to the parallel alignment of nanodisc with respect to the alternating current magnetic field, which is confirmed by good agreement between experimental results and micromagnetic simulation. It is found that such parallel alignment could enhance the SAR value by a factor of ≈2 with respect to the randomly oriented case. The above results indicate that the nanodisc provides an excellent thermal seed for magnetic hyperthermia. This study sheds the light on the magnetic hyperthermia mechanism of magnetic nanodisc and it also opens the window to explore high efficiency thermal seeds by controlling the orientation of magnetic nanostructures.

1. Introduction

Magnetic nanoparticle hyperthermia (MNH) is a promising therapeutic cancer treatment that kills the tumor cells. By exposure to an alternating current (AC) magnetic field, magnetic nanoparticles could generate heat and rise the temperature locally to above 42 °C at tumor cells.[1] Consequently, the tumor cells could be functionally damaged or even killed, while the normal cells are still alive because of better resistance to high temperature.[2] The MNH shows several advantages as compared with conventional therapeutics (i.e., surgery, chemotherapy, radiation therapy, etc.), such as high efficacy, low side effects, and more targeted localization in tumors.[3] The success of recent clinical trials has demonstrated the feasibility of this technique.[4] In MNH, the heat transfer ability of the nanoparticles (thermal seeds) is usually characterized by the specific absorption rate (SAR). The high SAR is a prerequisite for practical application, because it offers the possibility to minimize the side effect by reducing the particle concentration.[5] Therefore, many ongoing efforts are being devoted to develop high SAR heating agent.

In general, there are several factors that influence the magnetic hyperthermia performance of nanoparticles. First, changing composition is an effective way to enhance the SAR values at given experimental conditions. For example, metallic magnetic materials (i.e., Fe, FeCo) have high saturation magnetization (Ms) and they could achieve high SAR values.[6] It is reported that $CoFe_2O_4$ coated ferrite nanoparticles showed very high SAR values.[7] However, it should be emphasized that metallic nanoparticles are usually unstable at ambience. Meanwhile, introducing heavy element (i.e., Co, Mn) may cause toxicity.[8] For bio-applications, iron oxides (Fe_3O_4 or γ-Fe_2O_3) are the best choice because of excellent biocompatibility.[9] Second, in addition to the chemical composition, particles size and shape are another important optimization factors of achieving high SAR value without introducing toxic elements. Ferro-/ferri-magnetic nanoparticles can exhibit higher SAR values than the ultrafine superparamangetic nanoparticles due to larger hysteresis loss.[7,10] Additionally, different geometric shape leads to distinct shape anisotropy, resulting in significant difference in hysteresis loss and SAR value.[11] For instance, nanocube could give higher SAR than spherical nanoparticles.[12] Recently, Serantes et al. found that the chain-like arrangement biomimicking magnetotactic bacteria could exhibit better heating performance than the randomly distributed system, implying the crucial role of shape anisotropy.[13]

In recent years, disc-shape magnetic materials have attracted much attention. It is reported that the vibration of permalloy ($Fe_{20}Ni_{80}$) microdisc under low frequency magnetic field could kill tumor cells directly.[14] It motivates us to study the MNH of iron oxide nanodisc. To our best knowledge, there are limited reports on the hyperthermia properties of iron oxide nanodisc. Although Ma et al. showed some interesting results on Fe_3O_4 nanoplates, there is a lack of deep understanding on the hyperthermia properties.[15] On the other hand, the fabrication of high quality magnetic iron oxide nanodisc still remains

Dr. Y. Yang, X. Liu, Y. Lv, Dr. T. S. Herng, Dr. J. Fang, W. Xiao, Prof. J. Ding
Department of Materials Science and Engineering
National University of Singapore
117574, Singapore
E-mail: msedingj@nus.edu.sg

X. Xu, Prof. W. Xia, Prof. J. Ding
Ningbo Institute of Materials Technology and Engineering
Ningbo, Zhejiang 315201, China

X. Xu
Department of Physics
Sichuan Normal University
Chengdu 610066, China

T. Zhang
BioSystems and Micromechanics IRG
Singapore-MIT Alliance for Research and Technology
138602, Singapore

DOI: 10.1002/adfm.201402764

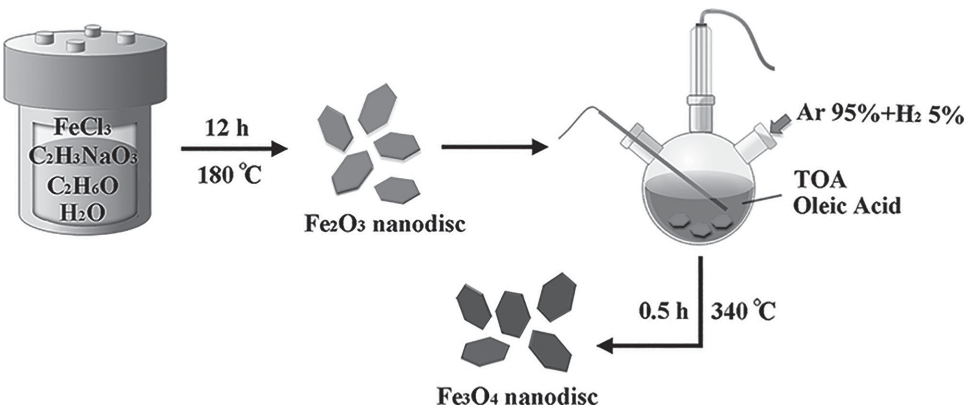

Figure 1. Schematic illustration for the synthesis of iron oxide nanodisc.

an open problem. To date, several hydrothermal methods have been reported for the synthesis of Fe_3O_4 nanoplates or nanoflakes.[15,16] However, the current methods could hardly achieve uniform size and disc shape, which makes it urgent to develop an effective method to synthesis uniform iron oxide nanodisc. In this work, we develop a two-step synthesis of iron oxide nanodisc and present a systematic study on its magnetic hyperthermia performances.

2. Results and Discussion

The two-step synthesis includes the fabrication of hematite (α-Fe_2O_3) nanodiscs by hydrothermal method and hydrogen-wet reduction, as illustrated in **Figure 1**. In the first step, uniform hexagonal α-Fe_2O_3 nanodiscs are fabricated by a hydrothermal method based on a facile alcohol-thermal reaction proposed by Chen et al.[17] These α-Fe_2O_3 nanodiscs are used as template and converted into Fe_3O_4 phase. In principle, this reduction process can be achieved by traditional thermal annealing in hydrogen gas. However, it usually requires a relative high temperature (above 420 °C),[18] which may lead to the shape damage or coalescence.[19] In contrast, the hydrogen-wet reduction method,[20] which is performed in the mixture of trioctylamine (TOA) and oleic acid (OA), could effectively avoid the coalescence because of a moderate reaction temperature (≈340 °C) and magnetic stirring effect during reduction process. Moreover, the OA could also prevent the aggregation of nanodisc as a traditional surfactant.[21] Thus, we combine the alcohol-thermal method with the hydrogen-wet reduction to fabricate high quality Fe_3O_4 nanodiscs.

Figure 2 presents the scanning electron microscopy (SEM) images of the synthesized nanodiscs before and after reduction. Before reduction, it is clearly seen in Figure 2a that thin and uniform hexagonal iron oxide nanodiscs are obtained on a large scale. After reduction process, the morphology and sizes of the products are well maintained, as shown in Figure 2b. More importantly, no obvious coalescence is observed, indicating the advantage of the hydrogen-wet reduction method over traditional thermal annealing method. The nanodisc is ≈26 nm thick (T) with a mean diameter (D) about 225 nm. The aspect ratio (D/T) is calculated to be 8.6, which implies strong shape anisotropy of the nanodisc. It should be mentioned that the amount of OA is crucial for the reduction of α-Fe_2O_3 nanodisc. Insufficient OA would cause incomplete reduction, while excessive OA could lead to the destruction of disc shape (see Figure S1, Supporting Information). An appropriate amount of OA is around 1 g for the reduction of 100 mg α-Fe_2O_3 nanodisc.

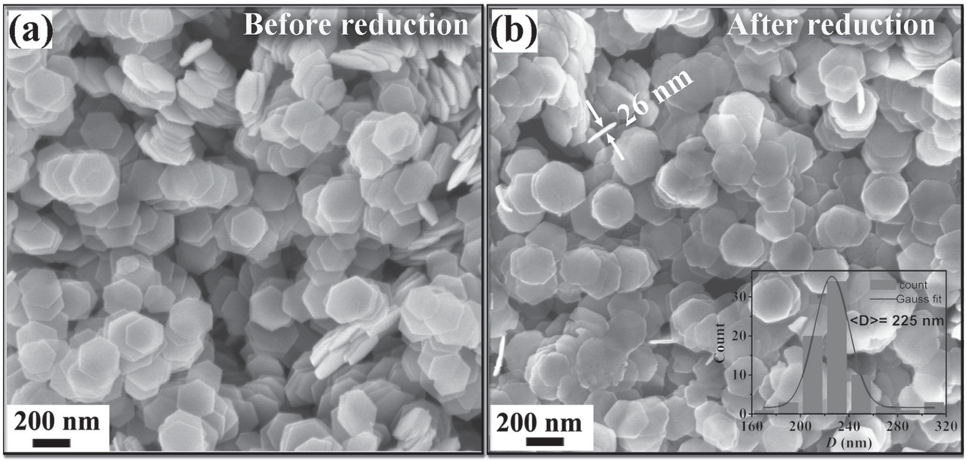

Figure 2. SEM images of iron oxide nanodiscs a) before and b) after reduction. The inset in b) is diameter distribution of the nanodiscs after reduction.

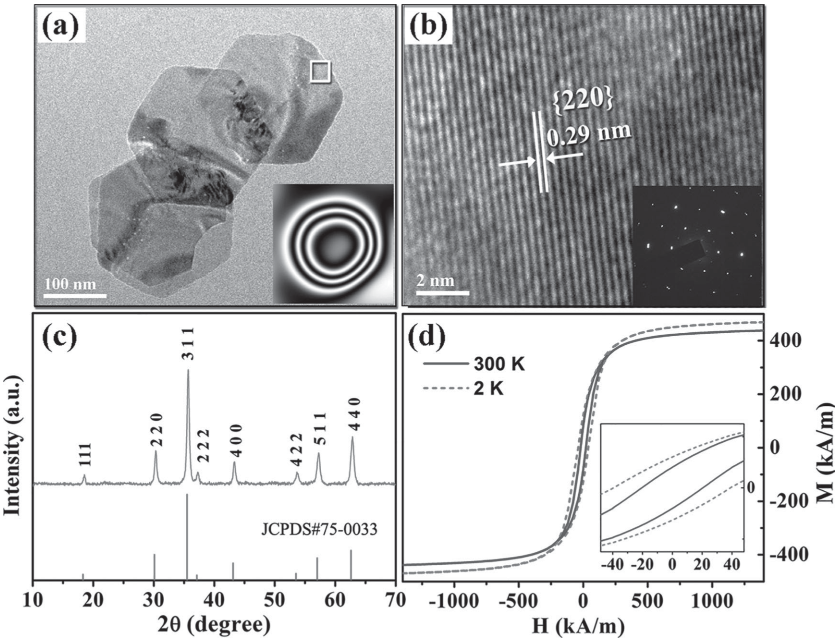

Figure 3. a) TEM, b) HRTEM, c) XRD pattern, and d) hysteresis loops of Fe_3O_4 nanodiscs. The insets in a) and b) are electron holography and SAED image of a single nanodisc, respectively.

Figure 3a shows the transmission electron microscopy (TEM) images of the nanodiscs after reduction process. As shown in the figure, the nanodiscs exhibit hexagonal shape. Moreover, electron holography (inset in Figure 3a) reveals closed magnetic flux within individual nanodisc, indicating the existence of vortex magnetic domain structure.[22] Such vortex domain structure is beneficial to the colloidal stability because the magnetic flux is mainly enclosed in the nanodisc, resulting in weak inter-discs magnetic dipole–dipole interaction.[14,23] High-resolution transmission electron microscopy (HRTEM) image was taken from the white square area in Figure 3a and presented in Figure 3b. It reveals a lattice spacing of 0.29 nm, which corresponds to the lattice spacing of (220) plane of inverse spinel Fe_3O_4.[24] The selected area electron diffraction (SAED, inset in Figure 3b) confirms the single-crystalline nature of the nanodisc after reduction. Figure 3c provides the typical X-ray diffraction (XRD) pattern of the nanodiscs after reduction. The pattern can be well indexed to Fe_3O_4 (JCPDS Card Nos. 75–0033). It is noted that characteristic peaks of γ-Fe_2O_3 (JCPDS Card Nos. 39–1346), such as (110), (210), and (211), are not observed even their relative intensities are higher than that of (111) peak, ruling out the presence of γ-Fe_2O_3 in our nanodiscs.[25] Furthermore, the relative intensity of (111) peak of the nanodisc is around 7%, which matches well with standard value of Fe_3O_4 (7%) and is obviously higher than that of γ-Fe_2O_3 (4%). More importantly, the zero field cooling-field cooling (ZFC-FC) curves (see Figure S2, Supporting Information) exhibit a prominent Verwey transition at about 110 K, a typical characteristic of Fe_3O_4, which is not observed for γ-Fe_2O_3.[26] These data clearly manifest the presence of pure Fe_3O_4 phase in our nanodiscs after reduction process. Figure 3d shows the hysteresis loops of the Fe_3O_4 nanodisc. It can be seen that the nanodisc exhibits ferrimagnetic behavior. At room temperature (300 K), the saturation magnetization (M_s) is about 435 kA m^{-1}. Meanwhile, the coercivity (H_c) is around 21.3 kA m^{-1}. It is more than two times higher than the reported value (about 7.9 kA m^{-1}) of isotropic Fe_3O_4 nanoparticle with similar size (≈114 nm).[27] This might be attributed to the shape anisotropy of nanodisc. At 2 K, the M_s increases slightly to about 467 kA m^{-1} (close to the bulk value of about 500 kA m^{-1})[28] and the H_c increases to around 39.0 kA m^{-1}.

To conduct the magnetic hyperthermia measurement, the Fe_3O_4 nanodiscs are dispersed into water using cetyltrimethylammonium bromide (CTAB) as the stabilizer. The success of CTAB coating is proved by fourier transform infrared (FT-IR) measurement (see Figure S3a, Supporting Information). After the coating process, the mean hydrodynamic size (d_{hyd}) of the nanodiscs is about 164 nm (Figure S3b, Supporting Information). This value is slightly higher than the equivalent diameter (≈125 nm) of the bare nanodisc, which indicates good dispersion of Fe_3O_4 nanodisc in aqueous suspension.

To better understand the hyperthermia performance of the nanodisc, we prepared two isotropic Fe_3O_4 nanoparticles as reference samples: superparamagnetic nanoparticles (SNP) and ferrimagnetic nanoparticle (FNP). The SNP is chosen because it is the most widely used thermal seed for MNH.[3a,29] **Figure 4**a (top) presents the TEM image of the SNP, showing that the mean diameter is about 11.2 nm (typical superparamagnetic nanoparticle). FNP is selected because it could offer much higher SAR values due to superior hysteresis loss.[30] Figure 4a (bottom) shows the SEM image of the FNP, exhibiting the mean size of about 58.7 nm. This value is close to the optimal size (≈60 nm) for the highest hysteresis loss.[30] Since the SNP and FNP are isotropic, their comparisons with anisotropic nanodisc could provide rich information in physics. In this work, the hyperthermia performances of all three samples are measured under identical conditions with 488 kHz AC magnetic fields. As illustrated in Figure 4b, the field is generated by a copper coil and the temperature rise is recorded by a temperature meter as a function of time. The field strength (H) is changed from 15.9 to 47.8 kA m^{-1}. It should be emphasized that the maximum product of the field strength and frequency ($H \times f$) in the measurement is $\approx 2.3 \times 10^{10}$ Am^{-1} s^{-1} , which is well below the upper limitation of 4.5×10^{10} Am^{-1} s^{-1} to avoid non-selective heating of both cancerous and healthy tissue due to eddy currents.[31] Based on the temperature-time curves (Figure S4, Supporting Information), the SAR values are evaluated. Figure 4c shows the SAR values of the three samples measured in aqueous suspension at different field H. As shown in the figure, the SAR values of SNP are below 1 kW g^{-1} at all these fields. For instance, it is about 0.42 kW g^{-1} at 31.8 kA m^{-1}. This value agrees well with the reported value of 0.35 kW g^{-1} for 12 nm Fe_3O_4 nanoparticles at similar experimental condition (≈36.6 kA m^{-1}, 500 kHz).[7] Apparently, the FNP displays obviously higher SAR values than the SNP because of larger hysteresis loss. More remarkably, the nanodiscs possess the highest SAR value of about 5 kW g^{-1} at 47.8 kA m^{-1}, which is more than 2 times higher than that of the FNP.

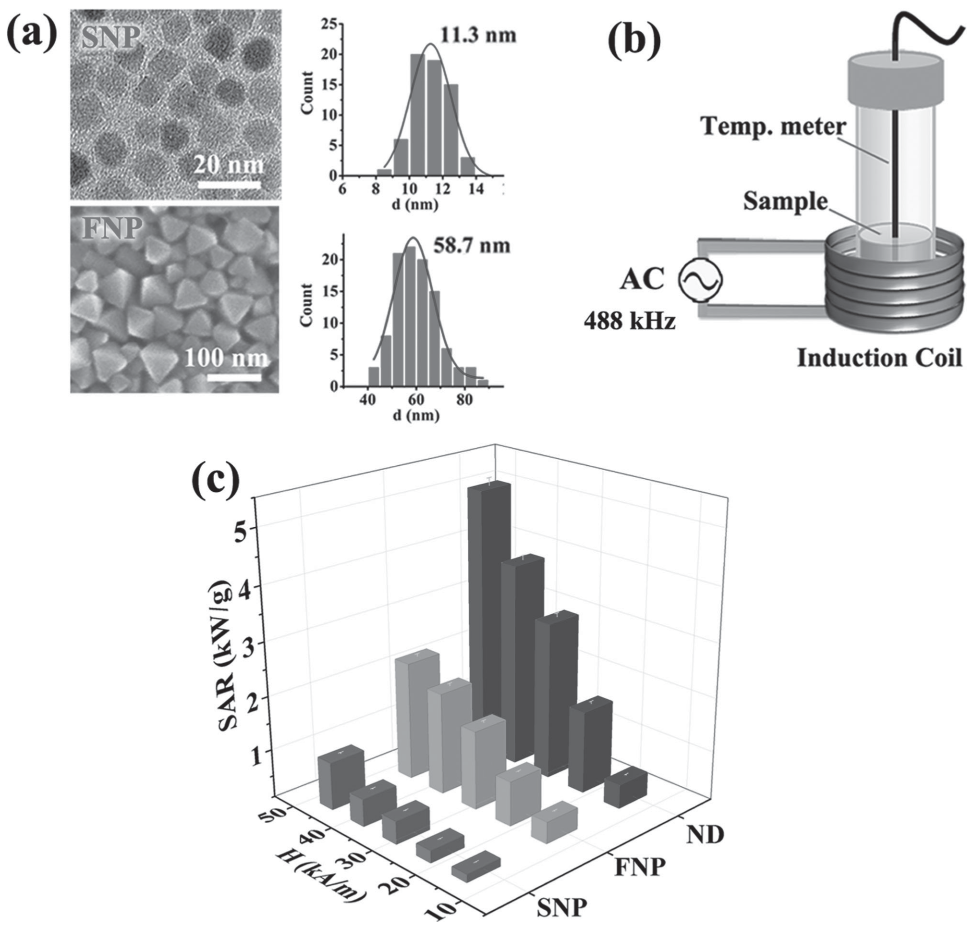

Figure 4. a) TEM and SEM images of reference samples, namely, Fe_3O_4 superparamagentic nanoparticles (SNP) and ferrimagentic nanoparticles (FNP), respectively. b) Illustration of experimental setup for hyperthermia testing. c) SAR values of Fe_3O_4 nanostructures measured at different AC magnetic field strengths H.

To verify the experimental results for FNP and nanodisc, we reproduce the SAR values at 47.8 kA m^{-1} using theoretical calculation. It is known that the major heating mechanism in MNH is hysteresis loss.[1,10,32] In principle, the hysteresis loss can be derived from the dynamic hysteresis loop at exactly the same frequency as used in hyperthermia experiment. For example, Carrey et al. proposed a theoretical model to calculate the dynamic hysteresis loop for fine single domain nanoparticles.[33] However, it is not applicable to calculate the large nanoparticles with multi-domain structures. Till now, there is a lack of general method to calculate the dynamic hysteresis loop of multi-domain nanoparticles. Nevertheless, we could perform micromagnetic simulation to simulate static hysteresis loop for estimation. This is reasonable for large nanoparticles (the size is well above the superparamagnetism critical size), because the switching time of magnetic moment is on order of 10^{-9} s (see Figure S5, Supporting Information), which is much shorter than the typical time (around 10^{-6} s) of field changing in MNH. As a result, the moment switching in large particle is sufficiently fast to follow the AC field. Therefore, we could simulate the static hysteresis loop to derive the SAR value for the FNP and nanodisc.

As different orientations may lead to distinct hysteresis behaviors,[34] magnetic hysteresis loops along different directions are simulated to imitate random orientation of nanoparticles in aqueous suspension. **Figure 5**a shows direction-dependent hysteresis loops of FNP which possesses a uniform magnetic domain along the easy axis (see Figure S6, Supporting Information). It can be seen from the figure that the hysteresis behavior strongly depends on the direction of external field. As illustrated in the inset, the angle between magnetic moment and external field H is defined as θ varying from 0° to 90° at an interval of 10°. Based on these loops, an average hysteresis loop is calculated by using

$$M_{\text{ave}} = \frac{\sum_{\theta} M_{\theta} * \sin\theta}{\sum_{\theta} \sin\theta} \tag{1}$$

where M_{ave} is the magnetization of the average loop, $M\theta$ is magnetization of the hysteresis loop simulated along θ direction. The factor sin θ is adopted as a spherical average weighting factor for a random orientation (see Figure S7, Supporting Information). Figure 5b shows the average loop of FNP calculated through Equation (1). Based on the average loop, the theoretical SAR value can be computed by[30,33]

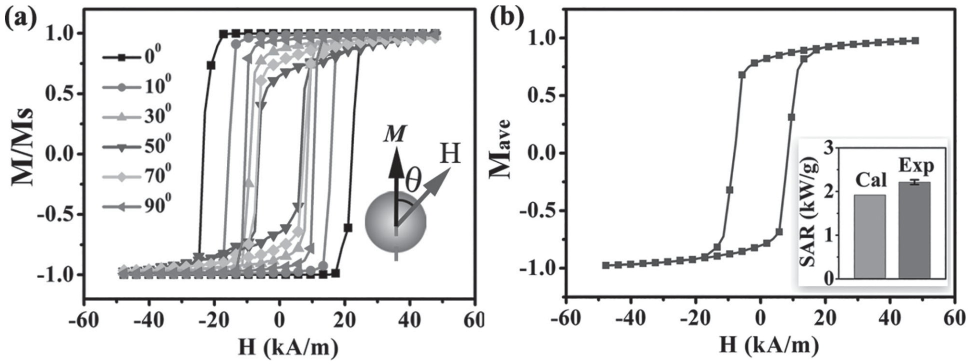

Figure 5. a) Simulated hysteresis loops of FNP along different directions. The inset shows the illustration of the relative angle θ between the magnetic moment and AC field. b) Calculated average hysteresis loop. The inset shows the comparison between the SAR value calculated from the average loop and that measured at 47.8 kA m^{-1}.

$$\mathrm{SAR}_{\mathrm{cal}} = \frac{1}{0.724}\frac{P}{\rho\varphi} \quad (2)$$

with

$$P = \mu_0 f \oint M \, \mathrm{d}H \quad (3)$$

where ρ is the density of Fe_3O_4 (5.17×10^3 kg m^3),[35] φ is the volume fraction of Fe_3O_4 (equals to 1 for one pure Fe_3O_4 particle), P is the heat dissipation due to hysteresis loss, μ_0 is vacuum permeability, f is the frequency (488 kHz) of the AC field, M is the magnetization ($M_s \cdot M_{ave}$). To be consistent with experiment, the experimental M_s value (418 kA m^{-1}) is used in the SAR calculation. It is worth noting that the term of 1/0.724 (0.724 is the weight fraction of Fe in Fe_3O_4) is included in above equation, as compared with the equation reported earlier.[30] This is to convert the unit of SAR value from Watt per gram of Fe_3O_4 to per gram of Fe element. Using Equations 2 and 3, the theoretical SAR value, corresponding to 488 kHz and 47.8 kA m^{-1} field, can be calculated. The calculated SAR value in Figure 5b is around 1.92 kW g^{-1}, which is slightly lower than the experimental value of 2.22 kW g^{-1}. This may be ascribed to the formation of dissipative structures due to the rotation of nanoparticle under applied AC magnetic field, increasing the SAR in aqueous suspension.[32] To exclude the influence of the above effect, the SAR value of FNP is measured in agarose gel (5%), where the rotation of FNP is suppressed as a result of immobilization.[36] The measurement shows that the SAR value in the gel suspension is around 1.91 kW g^{-1} at 47.8 kA m^{-1}, which is very close to 1.92 kW g^{-1} as calculated by our model. It indicates that our modeling works are well agreed with the experimental SAR value of FNP.

Figure 6a presents the simulated ground-state domain structure of the nanodisc. The majority of spins are aligning circularly in the plane of nanodisc, while the center ones are pointing out of plane, forming a typical vortex domain structure.[37] This agrees very well with the electron holography result (inset in Figure 3a). Starting from the vortex domain structure, the hysteresis loops are simulated along different directions, as illustrated in Figure 6b. Herein, the θ represents the angle between the magnetic field H and the normal direction of the nanodisc. Similar to the FNP, the nanodisc also exhibits direction-dependent hysteresis loops. For θ below 40° (including 40°), the loops are straight lines. In contrast, multi-switching takes place when θ is between 50° and 90°. Such multi-switching is attributed to the occurrence of metastable states during reversal process. Figure 6c presents the domain evaluation when H is parallel to the nanodisc ($\theta = 90°$). Obviously, the first switching at zero field corresponds to the transition from saturation state (i) to the *c*-state (ii).[38] With increasing H in the opposite direction, a vortex core moves in from the edge of the nanodisc and forming a vortex state (iii). The vortex core moves gradually toward the opposite edge when H increases further. The nanodisc is saturated until the vortex core disappears (iv). Based on these hysteresis loops, the average loop is calculated by using Equation 1, as depicted in Figure 6d. Finally, the SAR value is calculated to be 3.02 kW g^{-1} via Equations 2 and 3. However, it is noted that this value is much lower than the experimental value of about 5.01 W g^{-1} at 47.8 kA m^{-1} (Figure 5c). Such a noticeable discrepancy implies that the random orientation model is insufficient to calculate the SAR of the nanodisc in aqueous suspension. This might be related to the orientation change after applying the AC field. It is reported that magnetic micro-discs can be aligned parallel to external magnetic field when they are suspended in water.[14] Meanwhile, Mamiya et al. found that the rotation of elongated nanoparticles to high AC magnetic field could increase the hysteresis loss.[32] Hence, the alignment of our nanodiscs might be one of the possible explanations for the discrepancy between the calculated and experimental SAR values.

In order to verify the alignment of nanodisc in aqueous suspension, we direct a laser into the sample during hyperthermia measurement. **Figure 7**a shows the experimental setup. A 532 nm continuous wave laser beam is directed into the nanodisc aqueous suspension that is placed in the coil. The AC field is parallel to the laser beam. On the top of the coil, a silicon photon-diode is placed to detect the intensity of laser passing through the sample, which is monitored by an oscilloscope. Figure 7b presents the laser intensity variation as a function of AC field switching (on or off). It is obvious that the laser

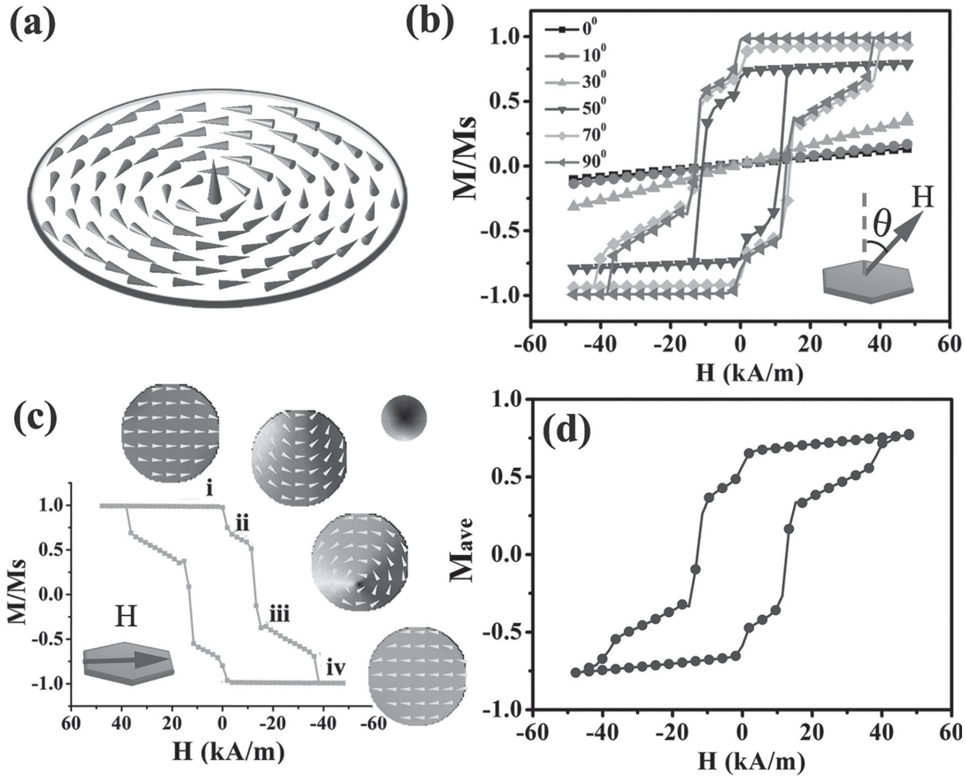

Figure 6. a) Simulated magnetic ground state and b) directional hysteresis loops of a single Fe_3O_4 nanodisc. c) Magnetic states during switching when field is parallel to nanodisc. d) Calculated average hysteresis loop of the nanodisc.

intensity changes synchronously with switching on or off for a period of 1 s. When the field (≈7.9 kAm^{-1}) is on, there is an abrupt increase (about 35%) in the laser intensity. When the field is off, the intensity gradually decreases to its initial level as before applying the field. Such phenomenon can be interpreted as follows: the parallel alignment allows most laser beam to pass through the sample (see Figure 7d), leading to the abrupt increase of detected beam intensity. In contrast, when the field is turned off, the parallel alignment is replaced by random orientation (Figure 7c) due to the Brownian motion.[39] As a result, the laser beam is partially blocked, leading to the decrease of beam intensity. The above results prove that the nanodisc can be aligned to the AC magnetic field in aqueous suspension during hyperthermia experiment. Therefore, the random

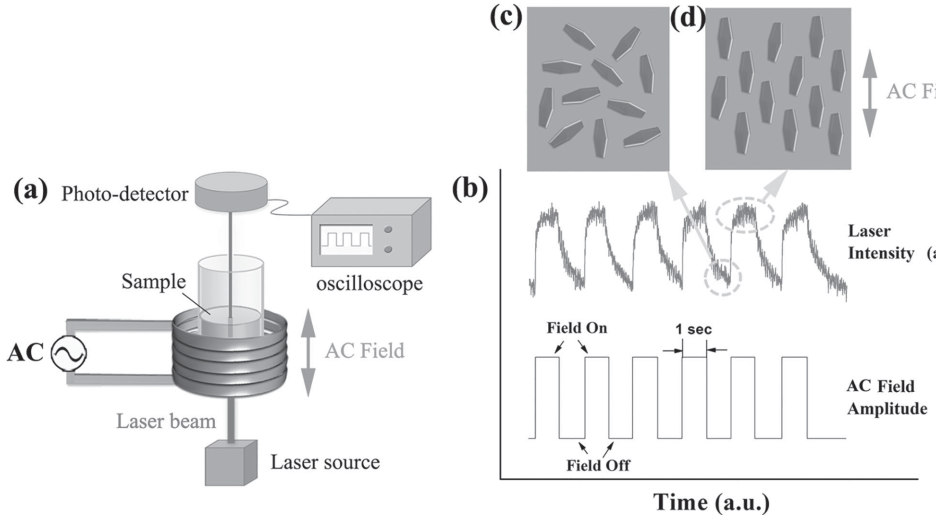

Figure 7. a) Experimental setup and b) detected intensity of a laser beam passing through the Fe_3O_4 nanodisc aqueous suspension when exposed in AC magnetic field. c,d) Illustration of field-driven nanodisc alignment.

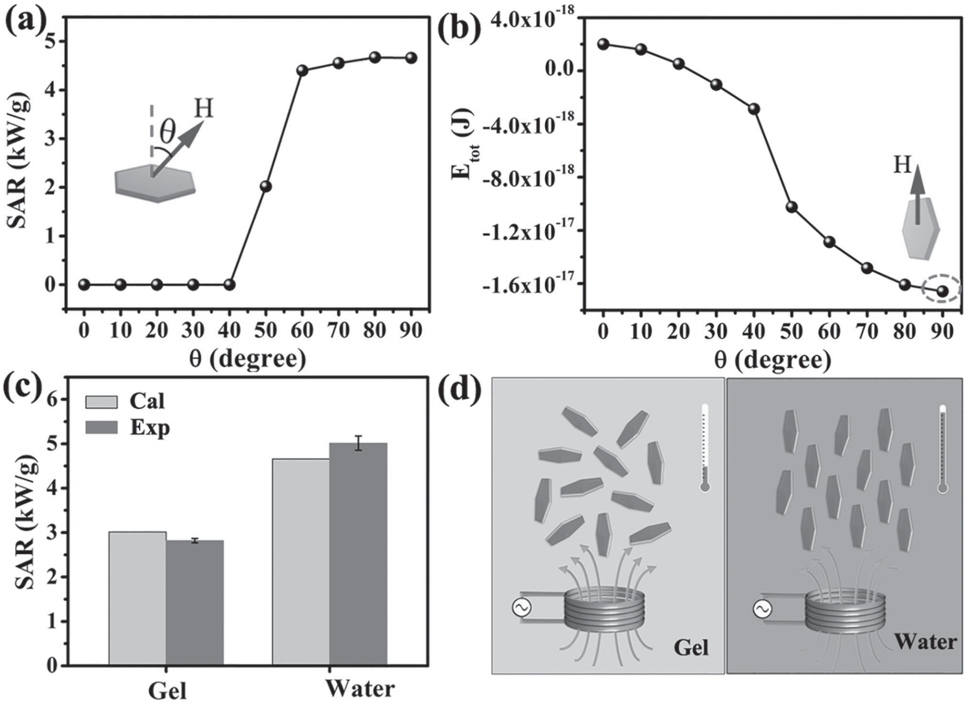

Figure 8. a,b) Calculated SAR values and total energy (E_{tot}) of the Fe_3O_4 nanodisc when field is applied along different directions. c) Comparison between experimental and calculated SAR values in gel and aqueous suspension when subjected into 47.8 kA m^{-1} and 488 kHz AC field. d) Illustration of orientations related magnetic hyperthermia of nanodisc in different suspensions.

orientation is invalid and the parallel alignment should be used in SAR calculation.

Figure 8a shows the simulated direction-dependent SAR values of nanodisc, which are derived from the hysteresis loops in Figure 6b. The SAR value changes dramatically with orientation. At low θ (0–40°), the SAR value is zero. This is because the hysteresis loops are straight lines (Figure 6b), associated with zero hysteresis loss. When θ is above 50°, the SAR rises quickly and reaches a plateau of around 4.4 kW g^{-1}. According to Figure 6b, the rapid increase in SAR should be ascribed to the occurrence of multi-switching hysteresis behavior. Figure 8b shows the simulated total energy (E_{tot}) when applying field H (47.8 kA m^{-1}) along different directions. It is clear that the E_{tot} decreases monotonically with increasing θ and it reaches the minimum at $\theta = 90°$, indicating that the parallel alignment of nanodisc with respective the field is energetically preferred. Moreover, the E_{tot} becomes negative when θ is larger than 20°, implying that the nanodisc can automatically rotate to the field for minimizing the energy. It is well agreed with the laser experiment observation in Figure 7. All the above results suggest that the SAR of nanodisc in aqueous suspension is predominated by its parallel orientation ($\theta = 90°$) with its SAR value of 4.66 kW g^{-1}. This value matches well with the experimental value of 5.01 W g^{-1} as measured in aqueous suspension (Figure 4c).

So far, it has been proved that the high SAR value of the nanodisc in aqueous suspension is due to the parallel alignment of nanodiscs with respect to AC field. In contrast, random oriented nanodiscs should exhibit lower SAR value. To confirm this speculation, the nanodiscs are suspended in agarose gel (5%). Owing to the immobilization in gel, the nanodiscs are unable to rotate accordance to the switching field during hyperthermia test. Thus, the random orientation should be predominated in the gel. According to the measurement, the SAR value of nanodisc in the gel is around 2.82 kW g^{-1} at 47.8 kA m^{-1} field, which matches very well with the calculated value of 3.02 W g^{-1} as derived earlier with the random orientation model. Figure 8c compares the experimental SAR value of nanodisc under various mediums (water or gel) and different calculation models (parallel alignment or random orientation). It is apparent that the SAR value of nanodiscs in gel suspension agrees well with the calculated SAR value using the random orientation model. While, the SAR value of nanodiscs in aqueous suspension shows a good consistency with that calculated SAR value via parallel alignment model. It indicates that the SAR value of nanodisc could be modulated effectively by controlling nanodiscs orientation. As illustrated in Figure 8d, the parallel alignment of nanodiscs with respective to the AC field achieves higher temperature rise than the random orientation. It is worthwhile to note that the high SAR can be maintained in a wide range of orientations, ranging from 60° to 90° (Figure 8a). The results indicate that the nanodiscs are not strictly required to be parallel to the AC field. The deviation of ±30° is allowed to achieve high SAR value. Such wide angle orientation is of great advantage for practical hyperthermia application. It should be mentioned that the isotropic FNP also shows direction-dependent SAR values (see Figure S8a, Supporting Information) due to the magnetocrystalline anisotropy. However, the E_{tot} is almost constant (Figure S8b, Supporting Information) compared with that of nanodisc. Therefore, the alignment effect of FNP is not as obvious as the nanodisc in hyperthermia measurement.

As mentioned earlier, high SAR value is achieved on Fe_3O_4 nanodisc by solely utilizing the shape anisotropy and no toxic elements (i.e., Co, Mn, etc.) are incorporated into nanodiscs. To test the biocompatibility of our Fe_3O_4 nanodiscs, we carried out a standard CKK viability test on MCF-7 cancer cells after 24 h incubation with the nanodiscs (see Figure S9, Supporting Information). The result shows that almost 90% cell viability is achieved after 24 h of incubation with Fe concentration of 50 μg mL^{-1}. For the Fe concentration of 100 μg mL^{-1} the cell viability slightly decreases to around 80% that is similar to the results reported on Fe_3O_4 nanoparticles.[40] The above results clearly indicate that good cytocompatibility is maintained, which makes the Fe_3O_4 nanodisc as a perfect material for bio-applications.

3. Conclusion

In summary, we have fabricated uniform Fe_3O_4 nanodiscs. The magnetic hyperthermia property of the nanodiscs were investigated by both experiment and micromagnetic simulation. By comparing with isotropic nanoparticles, it is found that the Fe_3O_4 nanodiscs could exhibit much better hyperthermia performance, which is attributed to the parallel alignment of nanodisc with respect to the AC field. This study indicates that the nanodisc can serve as an outstanding candidate of thermal seed for MNH.

4. Experimental Section

Synthesis of Fe_3O_4 Nanodisc: The synthesis includes two steps: In the first step, the α-Fe_2O_3 nanodisc template was prepared through facile alcohol–thermal reaction reported previously.[17] In a typical synthesis of α-Fe_2O_3 nanodiscs, 1.09 g $FeCl_3{\cdot}6H_2O$ and 2.8 mL distilled water were dissolved in ethanol (40 mL) by magnetic stirring. When completely dissolved, 5 g of sodium acetate was added into the mixture, which was then sealed in a Teflon-lined stainless steel autoclave and maintained at 180 °C for 12 h. After the mixture was cooled naturally to ambient temperature, the red precipitates were collected by centrifuge and washed with distilled water for several times then dried at 60 °C for further reduction. In the second step, The α-Fe_2O_3 nanodisc template was reduced into spinal Fe_3O_4 phase through a hydrogen-wet method.[20] In a typical reduction process, α-Fe_2O_3 nanodisc (100 mg) and trioctylamine (TOA; 20 g) were mixed by ultrasonic for 30 min, followed by addition of oleic acid (OA; 1 g). The mixture was fluxed at 340 °C under sufficient air flow of H_2 (5%) and Ar (95%) for about 30 min until the color changed to dark. After cooling to ambient temperature, the black product was collected by centrifuge and washed 3 times with toluene. Finally, the product was dried at 60 °C for characterization.

Characterization: The morphology and size of the product were characterized by a Hitachi S-4880 FESEM. The crystalline structure was characterized by XRD (Bruker, Advance D8) as well as HRTEM (JEOL-2010 at 200 kV). The electron holography experiment was carried out at a JEM-2100F TEM, which is equipped with a field emission gun and a specially designed object lens that can make the magnetic field at the specimen position less than 10 Oe. A biprism was installed to perform the holography experiment.[41] Magnetic hysteresis loops were measured using superconducting quantum interference device (SQUID, MPMSXL-5). FT-IR spectra of the CTAB modified Fe_3O_4 nanodisc were recorded using a Varian 3100 FT-IR (Excalibur series) spectrophotometer in the range 4000–400 cm^{-1} at a resolution of 4 cm^{-1}. The hydrodynamic size (d_{hyd}) of CTAB modified Fe_3O_4 nanodisc was characterized by dynamic light scattering (DLS, Malvern Zetasizer Nano-ZS).

Magnetic Hyperthermia Measurement: The hyperthermia performances of different Fe_3O_4 nanostructures were measured on an AC magnetic field generator (SPG-10-II, Shenzhen Shuangping). For the measurement, the nanostructures were dispersed into water using CTAB as the stabilizer. This is achieved by vigorous shaking the nanostructures in chloroform and the aqueous solution of CTAB, as described in ref. [42]. The agarose gel (5%) suspension was prepared by mixing the aqueous suspension (1 mL) with agarose gel (20 mg) at above 80 °C. In both the aqueous and gel suspensions, the weight fraction of iron (m_{Fe}) was kept as 0.1 mg mL^{-1}, which was determined by inductively coupled plasma (ICP) analysis. After measurement of temperature-time curves, SAR values were calculated by[43]

$$\mathrm{SAR}_{\mathrm{exp}} = C\frac{\Delta T}{\Delta t}\frac{1}{m_{\mathrm{Fe}}} \tag{4}$$

where C (4.18 J g^{-1} °C) is the specific heat of water or agarose gel.[44] $\Delta T/\Delta t$ donates the initial slope of the time-dependent temperature curve.[31b]m_{Fe} is the Fe concentration (0.1 mg mL^{-1}).

Micromagnetic Simulation Setup: The micromagnetic simulations were performed using the LLG Micromagnetics Simulator package.[45] In this package, the total energy (E_{tot}) of the ring magnet consists of five terms: exchange energy (E_{ex}), self-magnetostatic energy (E_s), magnetocrystalline anisotropy energy (E_k), surface anisotropy energy (E_{sk}), and Zeeman energy (E_{zee}). The magnetization distributions in magnetic nanostructures are obtained by solving Landau-Liftshitz-Gilbert-Langevin equation. The magnetic parameters of Fe_3O_4 used in the micromagnetic simulation are listed as follows: saturation magnetization M_s = 500 kA m^{-1}, exchange stiffness constant $A = 1.2 \times 10^{-11}$ J m^{-1}, magnetocrystalline anisotropy constant $K_1 = -1.35 \times 10^4$ J m^3, $K_2 = -0.44 \times 10^4$ J m^3.[23] The cell size is 4 nm. It is smaller than the exchange length (≈8.6 nm) as defined by $L_{ex} = (2A/\mu_0 M_s^2)^{0.5}$ to assure the accuracy of our simulation.[46] The Gilbert damping coefficient α was used as 0.5. To determine the ground states of magnetic nanostructures, we let the nanostructures relax in absence of applied magnetic field from the following either uniform magnetization or vortex state. The ground-state domain structure can be then determined after comparing the energy of different resultant equilibrium states. For the simulation of hysteresis loop, time-varying magnetic field is applied along certain directions with respective to the magnetic nanostructure. Meanwhile, the magnetization projections along these directions are recorded. Moreover, the simulation was performed at room temperature (300 K). Therefore, the thermal effect is included.

Cytotoxicity Test: MCF-7 breast cancer cells purchased from ATCC were cultured in DMEM (Dulbecco's Modified Eagle Medium) supplemented with 10% fetal bovine serum (FBS) at 37 °C in a humidified atmosphere containing 5% CO_2. Cells in log growing phase were used for the experiment. MCF-7 cells were seeded in 96-well plate at the density of 5 × 104 viable cells/well using DMEM containing 10% FBS, and incubated for 24 h to allow cell attachment. The media was removed and the replaced with fresh media. To each well, 200 μL magnetic suspensions with various Fe concentration (6.25–100 μg mL^{-1}) was added and incubated for 24 h. Untreated wells were used as control. At 24 h, 10 μL CCK-8 was added into the 96-well plates. The cells were incubated for another 4 h. The absorbance in each well was measured by microplate reader at 450 nm as reference using FluoStar Optima microplate reader.

Supporting Information

Supporting Information is available from the Wiley Online Library or from the author.

Acknowledgements

The project is financially supported by MOE Tier 2 R284–000–097–112, SERC 1321202068 (R284–000–105–305), NRF-CRP9–2011–01

(R284–000–111–592),NRF-CRP10-2012-02, A*Star SERC (R284-000-105-305), and Ningbo international cooperation projects 2012D10018.

Received: August 13, 2014
Revised: October 31, 2014

[1] R. E. Rosensweig, *J. Magn. Magn. Mater.* **2002**, *252*, 370.

[2] H. Sohn, R. H. Victora, *J. Appl. Phys.* **2010**, *107*, 09B312.

[3] a) S. Laurent, S. Dutz, U. O. Häfeli, M. Mahmoudi, *Adv. Colloid Interface Sci.* **2011**, *166*, 8; b) C. S. S. R. Kumar, F. Mohammad, *Adv. Drug Delivery Rev.* **2011**, *63*, 789; c) M. Creixell, A. C. Bohórquez, M. Torres-Lugo, C. Rinaldi, *ACS Nano* **2011**, *5*, 7124.

[4] F. K. H. van Landeghem, K. Maier Hauff, A. Jordan, K. T. Hoffmann, U. Gneveckow, R. Scholz, B. Thiesen, W. Brück, A. von Deimling, *Biomaterials* **2009**, *30*, 52.

[5] H. Rudolf, D. Silvio, M. Robert, Z. Matthias, *J. Phys.: Condens. Matter* **2006**, *18*, S2919.

[6] a) T. L. Kline, Y. H. Xu, Y. Jing, J. P. Wang, *J. Magn. Magn. Mater.* **2009**, *321*, 1525; b) L. M. Lacroix, R. B. Malaki, J. Carrey, S. Lachaize, M. Respaud, G. F. Goya, B. Chaudret, *J. Appl. Phys.* **2009**, *105*, 023911; c) Y. Jing, H. Sohn, T. Kline, R. H. Victora, J. P. Wang, *J. Appl. Phys.* **2009**, *105*, 07B305; d) B. Mehdaoui, A. Meffre, L. M. Lacroix, J. Carrey, S. Lachaize, M. Gougeon, M. Respaud, B. Chaudret, *J. Magn. Magn. Mater.* **2010**, *322*, L49.

[7] J. H. Lee, J. T. Jang, J. S. Choi, S. H. Moon, S. H. Noh, J. W. Kim, J. G. Kim, I. S. Kim, K. I. Park, J. Cheon, *Nat. Nanotechnol.* **2011**, *6*, 418.

[8] a) L. Horev-Azaria, G. Baldi, D. Beno, D. Bonacchi, U. Golla-Schindler, J. Kirkpatrick, S. Kolle, R. Landsiedel, O. Maimon, P. Marche, J. Ponti, R. Romano, F. Rossi, D. Sommer, C. Uboldi, R. Unger, C. Villiers, R. Korenstein, *Part. Fibre Toxicol.* **2013**, *10*, 32; b) J. Crossgrove, W. Zheng, *NMR Biomed.* **2004**, *17*, 544.

[9] D. Ling, T. Hyeon, *Small* **2013**, *9*, 1450.

[10] B. Mehdaoui, A. Meffre, J. Carrey, S. Lachaize, L. Lacroix, M. Gougeon, B. Chaudret, M. Respaud, *Adv. Funct. Mater.* **2011**, *21*, 4573.

[11] a) C. A. Ross, M. Farhoud, M. Hwang, H. I. Smith, M. Redjdal, F. B. Humphrey, *J. Appl. Phys.* **2001**, *89*, 1310; b) W. Zhang, S. Haas, *Phys. Rev. B* **2010**, *81*, 064433.

[12] C. Martinez Boubeta, K. Simeonidis, A. Makridis, M. Angelakeris, O. Iglesias, P. Guardia, A. Cabot, L. Yedra, S. Estrade, F. Peiro, Z. Saghi, P. A. Midgley, I. Conde Leboran, D. Serantes, D. Baldomir, *Sci. Rep.* **2013**, *3*, 1652.

[13] D. Serantes, K. Simeonidis, M. Angelakeris, O. Chubykalo Fesenko, M. Marciello, M. d. P. Morales, D. Baldomir, C. Martinez Boubeta, *J. Phys. Chem. C* **2014**, *118*, 5927.

[14] D. H. Kim, E. A. Rozhkova, I. V. Ulasov, S. D. Bader, T. Rajh, M. S. Lesniak, V. Novosad, *Nat. Mater.* **2010**, *9*, 165.

[15] M. Ma, Y. Zhang, Z. Guo, N. Gu, *Nanoscale Res. Lett.* **2013**, *8*, 1.

[16] X. Liu, S. W. Or, C. M. Leung, S. L. Ho, *J. Appl. Phys.* **2013**, *113*, 17B307.

[17] L. Chen, X. Yang, J. Chen, J. Liu, H. Wu, H. Zhan, C. Liang, M. Wu, *Inorg. Chem.* **2010**, *49*, 8411.

[18] a) H. M. Fan, J. B. Yi, Y. Yang, K. W. Kho, H. R. Tan, Z. X. Shen, J. Ding, X. W. Sun, M. C. Olivo, Y. P. Feng, *ACS Nano* **2009**, *3*, 2798; b) Y. L. Chueh, M. W. Lai, J. Q. Liang, L. J. Chou, Z. L. Wang, *Adv. Funct. Mater.* **2006**, *16*, 2243.

[19] S. Zhang, W. Wu, X. Xiao, J. Zhou, F. Ren, C. Jiang, *Nanoscale Res. Lett.* **2011**, *6*, 89.

[20] Y. Yang, X. Liu, J. Ding, *Sci. Adv. Mater.* **2013**, *5*, 1199.

[21] L. Zhang, R. He, H. Gu, *Appl. Surf. Sci.* **2006**, *253*, 2611.

[22] H. M. Fan, M. Olivo, B. Shuter, J. B. Yi, R. Bhuvaneswari, H. R. Tan, G. C. Xing, C. T. Ng, L. Liu, S. S. Lucky, B. H. Bay, J. Ding, *J. Am. Chem. Soc.* **2010**, *132*, 14803.

[23] Y. Yang, X. L. Liu, J. b. Yi, Y. Yang, H. M. Fan, J. Ding, *J. Appl. Phys.* **2012**, *111*, 044303.

[24] a) C. J. Jia, L. D. Sun, F. Luo, X. D. Han, L. J. Heyderman, Z. G. Yan, C. H. Yan, K. Zheng, Z. Zhang, M. Takano, N. Hayashi, M. Eltschka, M. Kläui, U. Rüdiger, T. Kasama, L. Cervera Gontard, R. E. Dunin Borkowski, G. Tzvetkov, J. R. Raabe, *J. Am. Chem. Soc.* **2008**, *130*, 16968; b) S. Laurent, D. Forge, M. Port, A. Roch, C. Robic, L. Elst, R. Muller, *Chem. Rev.* **2010**, *110*, 2574.

[25] W. Cheng, K. Tang, Y. Qi, J. Sheng, Z. Liu, *J. Mater. Chem.* **2010**, *20*, 1799.

[26] a) M. I. Dar, S. A. Shivashankar, *RSC Adv.* **2014**, *4*, 4105; b) G. F. Goya, T. S. Berquó, F. C. Fonseca, M. P. Morales, *J. Appl. Phys.* **2003**, *94*, 3520; c) W. Friedrich, *J. Phys.: Condens. Matter* **2002**, *14*, R285; d) T. J. Daou, G. Pourroy, S. Bégin-Colin, J. M. Grenèche, C. Ulhaq-Bouillet, P. Legaré, P. Bernhardt, C. Leuvrey, G. Rogez, *Chem. Mater.* **2006**, *18*, 4399; e) X. L. Huang, Y. Yang, J. Ding, *Acta Mater.* **2013**, *61*, 548.

[27] L. Li, Y. Yang, J. Ding, J. Xue, *Chem. Mater.* **2010**, *22*, 3183.

[28] G. Dionne, *Ferrimagnetism*, Springer, New York, **2009**.

[29] M. K. Yu, Y. Y. Jeong, J. Park, S. Park, J. W. Kim, J. J. Min, K. Kim, S. Jon, *Angew. Chem. Int. Ed.* **2008**, *47*, 5362.

[30] S. H. Noh, W. Na, J. T. Jang, J. H. Lee, E. J. Lee, S. H. Moon, Y. Lim, J. S. Shin, J. Cheon, *Nano Lett.* **2012**, *12*, 3716.

[31] a) R. Hergt, S. Dutz, *J. Magn. Magn. Mater.* **2007**, *311*, 187; b) D. Maity, P. Chandrasekharan, C. Yang, K. Chuang, B. Shuter, J. M. Xue, J. Ding, S. S. Feng, *Nanomedicine* **2010**, *5*, 1571.

[32] H. Mamiya, B. Jeyadevan, *Sci. Rep.* **2011**, *1*, 157.

[33] J. Carrey, B. Mehdaoui, M. Respaud, *J. Appl. Phys.* **2011**, *109*, 083921.

[34] F. Q. Zhu, G. W. Chern, O. Tchernyshyov, X. C. Zhu, J. G. Zhu, C. L. Chien, *Phys. Rev. Lett.* **2006**, *96*, 027205.

[35] J. Shin, K. M. Lee, J. H. Lee, J. Lee, M. Cha, *Integr. Biol.* **2014**, *6*, 532.

[36] R. Hergt, R. Hiergeist, I. Hilger, W. A. Kaiser, Y. Lapatnikov, S. Margel, U. Richter, *J. Magn. Magn. Mater.* **2004**, *270*, 345.

[37] Y. Gaididei, D. D. Sheka, F. G. Mertens, *Appl. Phys. Lett.* **2008**, *92*, 109910.

[38] D. Goll, G. Schütz, H. Kronmüller, *Phys. Rev. B* **2003**, *67*, 094414.

[39] D. B. Reeves, J. B. Weaver, *J. Appl. Phys.* **2012**, *112*, 124311.

[40] Y. Yang, X. Liu, Y. Yang, W. Xiao, Z. Li, D. Xue, F. Li, J. Ding, *J. Mater. Chem. C* **2013**, *1*, 2875.

[41] M. A. Schofield, M. Beleggia, Y. Zhu, G. Pozzi, *Ultramicroscopy* **2008**, *108*, 625.

[42] A. Swami, A. Kumar, M. Sastry, *Langmuir* **2003**, *19*, 1168.

[43] I. Hilger, K. Frühauf, W. Andrä, R. Hiergeist, R. Hergt, W. A. Kaiser, *Acad. Radiol.* **2002**, *9*, 198.

[44] X. L. Liu, E. S. G. Choo, A. S. Ahmed, L. Y. Zhao, Y. Yang, R. V. Ramanujan, J. M. Xue, D. D. Fan, H. M. Fan, J. Ding, *J. Mater. Chem. B* **2014**, *2*, 120.

[45] For more information on M. R. Scheinfein, LLG Micromagnetics Simulator User's Guide, http://llgmicro.home.mindspring.com/ (accessed: August 2014).

[46] a) C. A. F. Vaz, C. Athanasiou, J. A. C. Bland, G. Rowlands, *Phys. Rev. B* **2006**, *73*, 054411; b) R. D. McMichael, B. B. Maranville, *Phys. Rev. B* **2006**, *74*, 024424.